In Search of the Best Solid Electrolyte-Layered Oxide Pairing for Assembling Practical All-Solid-State Batteries

Tuncay Koç, Florencia Marchini, Gwenaëlle Rousse, Romain Dugas, Jean-Marie Tarascon

In the Search for the Best Solid Electrolyte-Layered Oxide Pairing for Assembling Practical All-Solid-State Batteries

Tuncay Koç[1,2,3], Florencia Marchini[1,3], Gwenaëlle Rousse[1,2,3], Romain Dugas[1,3] and Jean-Marie Tarascon[1,2,3,*]

1. Collège de France, Chaire de Chimie du Solide et de l'Energie, UMR 8260, 11 place Marcelin Berthelot, 75231 Paris Cedex 05, France

2. Sorbonne Université – 4 place Jussieu, F-75005 Paris, France

3. Réseau sur le Stockage Electrochimique de l'Energie (RS2E), FR CNRS 3459, 80039 Amiens, France

*Corresponding author: jean-marie.tarascon@college-de-france.fr

Abstract

All-solid-state batteries (ASSBs) are the subject of large enthusiasm as they could boost by 50% the energy density of today's Li-ion batteries provided that several fundamental/practical roadblocks can be solved. Focusing on the interface between the solid electrolyte and cathode active material (CAM), we herein studied the chemical/electrochemical compatibility of coated-layered oxide $LiNi_{0.6}Mn_{0.2}Co_{0.2}O_2$ with the three main inorganic electrolytes contenders, these being lithium thiophosphate (β-Li_3PS_4), argyrodite (Li_6PS_5Cl), and halide (Li_3InCl_6). Such electrolytes were prepared by either solvent-free or solution chemistry and paired with the CAM to form a composite which was further tested by assembling solid-state batteries using $Li_{0.5}In$ as negative electrode. Amongst the electrolytes prepared by dry routes, the best performing was found to be Li_6PS_5Cl followed by β-Li_3PS_4 and lastly Li_3InCl_6. In contrast, no general trend of benefit or detriment was observed when switching to solution route as it resulted in either performance improvement or deterioration depending on the electrolyte. Additionally, we show a strong dependence of the battery performance upon the presence of carbon additives. Lastly, we unraveled a pronounced chemical/electrochemical incompatibility of Li_3InCl_6 towards Li_6PS_5Cl and β-Li_3PS_4, hence questioning the design of hetero-structural cell architectures. Altogether, we hope these findings to provide guidance in the proper pairing of electrode-electrolytes components for designing highly performing solid-state batteries.

Keywords

Solid-state battery, solid electrolyte, sulfides, halides, solvent-based synthesis, solvent-free synthesis, coated layered oxide, cathode composite

Introduction

All-solid-state batteries (ASSBs) are generating worldwide excitement among research institutions, battery makers and users as evidenced by the increasing volume of related scientific publications and daily announcements by various start-ups. This excitement was initiated back to 2011 by the discovery of an inorganic sulfide-based electrolyte ($Li_{10}GeP_2S_{12}$) whose ionic conductivity of 10^{-2} S/cm^{-1} was comparable to the best Li-based liquid electrolytes.[1]

ASSBs are solvent-free devices, which offer safety advantages over lithium-ion systems while being theoretically capable of achieving a nearly 70% and 40% increase in volumetric (Wh/l) and gravimetric (Wh/kg) energy densities, respectively, taking advantage of Li-metal and bipolar cell configurations.[2] However, for this to happen several roadblocks dealing with problematic electrode-electrolytes chemical-electrochemical compatibilities at both negative and positive electrodes need to be equally addressed.[3–5] Various strategies relying on Li-surface engineering or on the use of Li-alloying coatings (Li_xAu, etc.) acting as buffer interfaces have been tried.[6] The best results achieved so far have been obtained with "anodeless" ASSBs in which the Li-metal anode is replaced by a silver-carbon composite electrode.[7] Positive electrodes of today's ASSBs are composites of a cathode active material (CAM, typically coated layered oxides) mixed with solid-ionic conductors and eventually carbon additives.[8,9] Their long cycling stability is presently plagued by chemical/electrochemical incompatibility issues between the oxide and the solid Li^+ conductor resulting in occasional decomposition reactions taking place at the interfaces.[10,11] The degree of advancement of such decomposition reactions depends upon the quality of oxide coating but more so on the nature of the solid ionic conductor used.[12–14]

Nowadays, a wide panel of fast Li^+ conductors for solid-state battery applications are known. The lithium thiophosphate family is probably the largest and one of the most attractive for practical applications. It enlists typical structures such as β-Li_3PS_4 from the Li_2S-P_2S_5 binary system, the argyrodite-type phases (Li_6PS_5X, X=Cl, Br and I) and the $Li_{10}GeP_2S_{12}$ phases together with its derivatives obtained by partial substitution of Ge or S. Despite the latter exhibits the highest ionic conductivities, it is also the most unstable thermodynamic-wise and ruled out for practical ASSBs.[15] More recently, halide-type ionic conductors Li_3MX_6 (M=In and trivalent rare earth metals Er, Y, etc., X=Cl, Br and I) have been revisited owing to their high ionic conductivity (10^{-4} - 10^{-3} S/cm)[16] and high stability against oxidation as deduced by density functional theory (DFT) calculations[17] and confirmed experimentally[18,19]. New electrolyte compositions such as $Li_2Sc_{2/3}Cl_4$ and Li_3ScCl_6 have been recently uncovered.[20,21]

Such richness of ionic conductors simultaneously represents a benefit and a hassle when selecting the best suitable solid electrolyte for pairing with a layered oxide positive electrode. Different electrolyte

chemistries indeed differ in their thermodynamic stability against oxidation and reduction, in their electronic and ionic conductivity, in their softness (which is higher for halides than for argyrodite and thiophosphates) and lastly in their thermal stability.[22] Moreover, their chemical-physical properties were also shown to depend on their synthesis method, either via solvent assisted reactions involving precipitation/crystallization in organic solvents, high temperature solid-state reactions (>500 °C) or mechanical ball milling followed by annealing steps.[23–26] Among them, the solvent-based routes appear to be particularly attractive for solid electrolyte (SE) - CAM composite preparation in a core-shell like structure (namely SE-coated oxide) by maximizing the energy density at electrode level while enhancing ionic percolation and boosting the cell performance.[27–29] However, in practice, such solution processes were shown to lead to phase contaminations or surficial remaining solvent species on solid ionic conductors.[30,31] Most of these aspects have already been addressed for most of ionic conductors independently and almost no cross-comparison between such studies have been made, with the exception of a recent study on halides that report their stability against argyrodite.[32]

Thus to fill this gap, we decided to embark ourselves in a benchmarking study of solid-state batteries using coated-$LiNi_{0.6}Mn_{0.2}Co_{0.2}O_2$ as part of a composite positive electrodes also including β-Li_3PS_4, Li_6PS_5Cl and Li_3InCl_6 as solid electrolytes. The latter were prepared either by solution or by solvent-free synthesis. For each electrolyte, we firstly studied the interplay between synthesis strategy, ionic/electronic conductivity and structural properties and later tested their performances in full all-solid-state batteries. The use of carbon additives together with the design of hetero-structural cell architecture were also explored. Through this survey, we found that the carbon containing coated-$LiNi_{0.6}Mn_{0.2}Co_{0.2}O_2$/argyrodite ($Li_6PS_5Cl$, synthesized by solid-state method) pair gave the best electrochemical cycling performance with a sustained reversible discharge capacity of 141 $mAh.g^{-1}$ as well as less than 3% decay upon 20 cycles.

Experimental Section

Solid Electrolyte Synthesis

The solvent-mediated synthesis of β-Li_3PS_4 solid electrolyte was prepared in tetrahydrofuran (THF). Stoichiometric amounts of Li_2S (Alfa Aesar, purity 99 w/w %) and P_2S_5 (Acros Organics, purity > 98 w/w %) were dispersed in THF (Sigma Aldrich, 99.9 % v/v). The precursors were stirred continuously for 48 h at room temperature and the powder was later recovered by centrifugation at 600 rpm for 3 min. Next, the

obtained powder was placed in a cylindrical Schlenk flask and dried at 100 ºC (heating rate 5 ºC/min) for 24 h and subsequently at 155 ºC for 24 h under dynamic vacuum (P < 0.1mbar).

The solvent-free β-Li_3PS_4 solid ion conductor was synthesized by mechanochemical milling of a stoichiometric mixture of Li_2S and P_2S_5 using planetary ball-mill followed by annealing step. The mixture of precursors was placed in a ZrO_2 jar of 45 mL together with 12 ZrO_2 balls (10 mm diameter, 3 g each). Ball to powder weight ratio was 36 : 1. The mixture was milled at 510 rpm for 20 h applying 15 min milling followed by 15 min of cooling step. The ball-milled powder was later pelletized and annealed at 200 ºC (heating rate 5 ºC/min) for 1 h in a quartz tube sealed under vacuum. After the annealing process, the sample was cooled naturally.

The solvent-engineered Li_6PS_5Cl was synthesized in THF/Ethanol solvents. Firstly, a suspension of Li_3PS_4.xTHF/THF was prepared by stirring of stoichiometric mixture of Li_2S and P_2S_5 in THF at room temperature for 48 h. Next, stoichiometric mixture of Li_2S and LiCl (Alfa Aesar, anhydrous, 99 wt. %) was dissolved in ethanol and further stirred at room temperature for 24 h. After the stirring processes, the suspension was transferred to the solution and greenish clear solution was obtained. The final greenish solution was later left stirring continuously overnight and further centrifuged at 600 rpm for 3 min to remove unreacted particles. Finally, the greenish clear solution was dried under dynamic vacuum (P < 1 mbar) to remove the solvent and then, a yellowish powder was obtained. The powder was introduced to a cylindrical Schlenk flask for further drying at 100 ºC for 24h and subsequently at 155 ºC for 48 h under dynamic vacuum (P < 0.1mbar). Next, the powder was pelletized and annealed at 550 ºC (heating rate 5 ºC/min) for 6 h in a quartz tube sealed under vacuum. The pelletized sample was cooled naturally after the annealing step.

The solid-state synthesis of Li_6PS_5Cl was carried out by annealing of stoichiometric mixture of Li_2S, P_2S_5 and LiCl in a Al_2O_3 crucible. The powder mixture placed in the crucible was sealed under vacuum in a quartz tube and finally, annealed at 550 ºC (heating rate 5 ºC/min) for 72 h followed by natural cooling.

The water-assisted synthesis of Li_3InCl_6 was prepared by dissolution of $InCl_3$ (Alfa Aesar, anhydrous, 99,99 w/w %) and LiCl in distilled water. The precursors were left stirring overnight continuously at room temperature and the clear solution was naturally dried at 100 ºC. Following the process, white powder was obtained and subsequently it was further dried at 100 ºC for 24 h and later at 200 ºC for 24 h under dynamic vacuum (P < 1mbar) followed by natural cooling.

The solvent-free Li_3InCl_6 solid ion conductor was synthesized by mechanochemical milling of a stoichiometric mixture of $InCl_3$ and LiCl using planetary ball-mill followed by annealing step. The ball-mill apparatus were used as explained above for solvent-free synthesis of β-Li_3PS_4 solid ion conductor. The

milling process was set at 510 rpm for 24 h applying 15 min milling followed by 15 min of cooling step. After the ball-milling process, the obtained powder was pelletized and annealed at 260 ^{o}C (heating rate 5 ^{o}C/min) for 5 h in a quartz tube sealed under vacuum. After the annealing process, the sample was cooled naturally.

Synthesis of core-shell-like cathode composites

β-Li_3PS_4-coated NMC622 particles were synthesized as follows. A mixture of Li_2S (0.115 mg), P_2S_5 (0.185 mg) and coated-NMC622 (700 mg) was transferred in THF (in a ratio of 35 mg of Li_2S and P_2S_5 solid particles per milliliter of solvent) and stirred for 48 hours at room temperature and subsequently, VGCF particles (50 mg) were added into the suspension by aiming a cathode composite in 70:30:5 wt% (coated-NMC622:β-Li_3PS_4:VGCF). The solid particles were collected by centrifugation at 600 rpm for 5 min and heated at 100 ^{o}C for 24h and then 155 ^{o}C for 24 h under vacuum.

Li_6PS_5Cl-coated NMC622 cathode composite was synthesized in the same line of the solvent-mediated synthesis of Li_6PS_5Cl solid electrolyte. Firstly, a suspension of Li_3PS_4.xTHF/THF was obtained at room temperature and next, the obtained suspension was transferred into a solution containing dissolved LiCl and Li_2S in ethanol. Next, coated-NMC622 (700 mg) was added into the greenish solution and stirred for 2 h at room temperature. Finally, the solution containing cathode active materials and Li_6PS_5Cl was dried to remove the solvent at 100 ^{o}C for 24h and later at 155 ^{o}C for 48 h under vacuum.

Li_3InCl_6-coated NMC622 particles were obtained using the dissolution of Li_3InCl_6 particles (300 mg) in THF. After 5 minutes of exposure, coated-NMC622 (700 mg) particles were transferred into the clean solution and stirred for 1 h. Finally, the solution containing cathode active materials and dissolved Li_3InCl_6 was heated first at 100 ^{o}C for 24 h and then at 200 ^{o}C for 24 h under vacuum to dry the solvent.

Conductivity measurements

The solid electrolyte samples were pelletized at 4 t/cm^2 during 5 minutes in an 8 mm die set and later transferred to the testing cell for the ionic and electronic conductivity measurements. Ionic conductivity measurements were performed by electrochemical impedance spectroscopy (EIS) at OCV applying excitation amplitude of 50 mV in a frequency range between 7 MHz – 1 Hz with 15 points per decade with MTZ impedance analyzer (BioLogic). Electronic conductivity measurements were measured by direct-current (DC) polarization on the pelletized solid electrolytes with applied voltages of 0.25 V, 0.50 V, 0.75 V and 1 V for 60 min each using a low current channel (BioLogic).

Characterization

Synchrotron X-ray powder diffraction (SXRD) patterns collected at the SOLEIL Synchrotron (St Aubin, France) on the CRISTAL beamline equipped with the Dectris Mythen dectector. All SXRD patterns were collected in transmission mode with $\lambda = 0.58185$Å, with the powder sealed in a glass capillary of diameter 0.7 mm. The refinements of the patterns were done using the Rietveld method as implemented in the FullProf program. Laboratory X-ray powder diffraction (XRD) were performed in an airtight cell equipped with a Be window. XRD patterns were recorded in reflection mode in Bragg−Brentano geometry using a Bruker D8 Advance diffractometer equipped with a Cu-K_α X-ray source ($\lambda_1 = 1.54056$ Å, $\lambda_2 = 1.54439$ Å) and a LynxEye detector.

Scanning electron microscopy (SEM)

Solid electrolyte and core-shell cathode composite micrographs were obtained on FEI Magellan scanning electron microscope equipped with an Energy dispersive X-ray spectroscopy (EDX) Oxford Instrument detector. EDX of the composite cathode was carried out using an acceleration voltage of 20 kV.

Battery assembling and electrochemical testing

The battery assembly and electrochemical testing were carried out in a cell, which was developed in our laboratory and consisting of a cylindrical polyetherimide (PEI) cell body and two stainless steel pistons of 8 mm diameter.

The two-electrode cell was assembled as follows. 30 mg of solid electrolyte were firstly added into the cell and cold pressed at 1 t/cm^2 for few seconds under a hydraulic press. 16 to 18 mg/cm^2 of cathode composite(coated-NMC622/SE/VGCF, 70:30:5 wt%) was then spread onto one side of the pre-compressed solid electrolyte and next, a mixture of $Li_{0.5}In$ and solid electrolyte (in a 60:40 weight ratio) was added onto other side of the solid electrolyte pellet as counter electrode. Finally, the whole stack was further densified at 4 t/cm^2 for 15 minutes. After the compression, the fully assembled cell was later closed with a torque key applying 2.3 Nm torque in each screw, which yields an internal pressure of 1 t/cm^2. All assembling procedures were carried out under argon atmosphere in a glove box ($[O_2] < 1$ ppm, $[H_2O] < 1$ ppm).

The three-electrode cell setup was modified from two electrode cell by placing 15 µm Al metal foil as RE current collector between two PEI body parts and the cell assembly was realized as explained in our previous work.[33]

Galvanostatic cycling studies were carried out in the voltage range of 2.1 - 3.6 V vs. LiIn/In at room temperature at C/20 (C correspond to 1 mole of Li per mole of active material in 1 h). Three-electrode full-cell impedance spectra were measured upon galvanostatic cycling at 3.2 V, 3.4 V, 3.6 V, 3.4 V, 3.2 V and

2.1 V after 4 h rest at each point using a 10 mV sinusoidal perturbation. 10 points per decade were taken for frequencies between 1 MHz - 10 mHz.

All electrochemical measurements were conducted with a VMP3 potentiostat/galvanostat (BioLogic) controlled with EC-Lab software.

Results and Discussion

Pure solid electrolytes

β-Li_3PS_4, Li_6PS_5Cl and Li_3InCl_6 powders were synthesized via solvent-assisted and solvent-free methods according to experimental protocols derived from the literature (see experimental section) and will be herein denoted with the prefixes **W-** and **C-**, respectively (Figure 1). The solid electrolytes were first characterized for their structure, morphology and electronic-ionic conduction by XRD, SEM and EIS spectroscopy, respectively. The collected XRD patterns (Figure 2a, b and c) match those already reported and indicate that nearly all the samples are pure phases. As expected, a greater broadening of the peaks was observed for samples made by mechanical ball milling given that this route promotes microstructural defects and particle nano-sizing. It is to note that Li_6PS_5Cl can be prepared as single phase by solid-state reaction, as opposed to the solution route, which also yields several crystalline impurities (see symbols in figure 2b) identified as Li_3PO_4, Li_2S and LiCl (Figure S1). Such a difficulty was also mentioned in the literature and associated to the interaction between PS_4^{3-} unit and ethanol.[26,31]

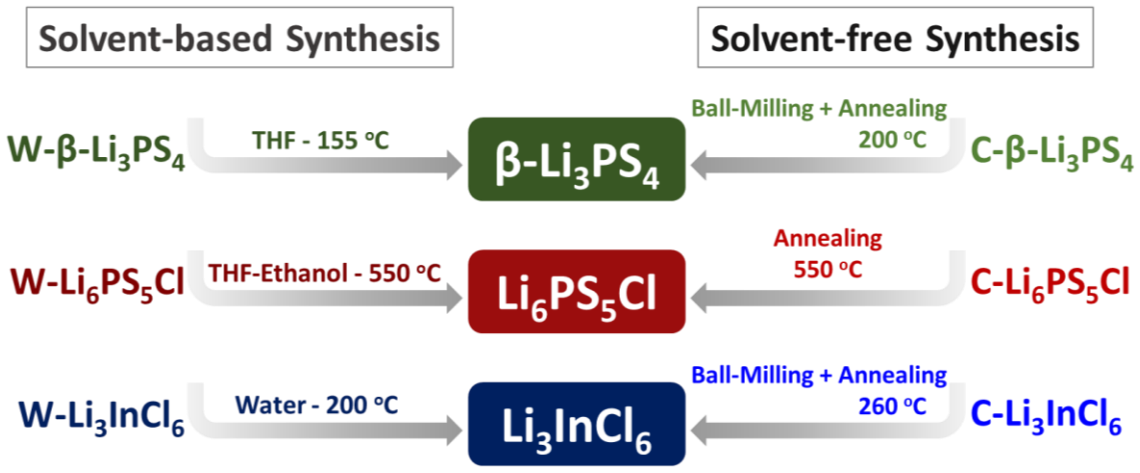

Figure 1: Synthesis routes and abbreviations used for studied solid electrolytes.

Figure 2d-i shows the SEM micrograph of the synthesized powders whose particles adopt various shapes depending upon the electrolyte chemistry. Particle morphology is nearly independent of the synthesis strategy for the halides in contrast to the noticeable differences for β-Li_3PS_4 and Li_6PS_5Cl when prepared by solid-state and wet route. The relative density of pelletized solid electrolytes (SEs) was also calculated, revealing that solvent-free route seems to facilitate the material densification enabling a porosity decrease down to ~5% for Li_3InCl_6 (Figure S2).

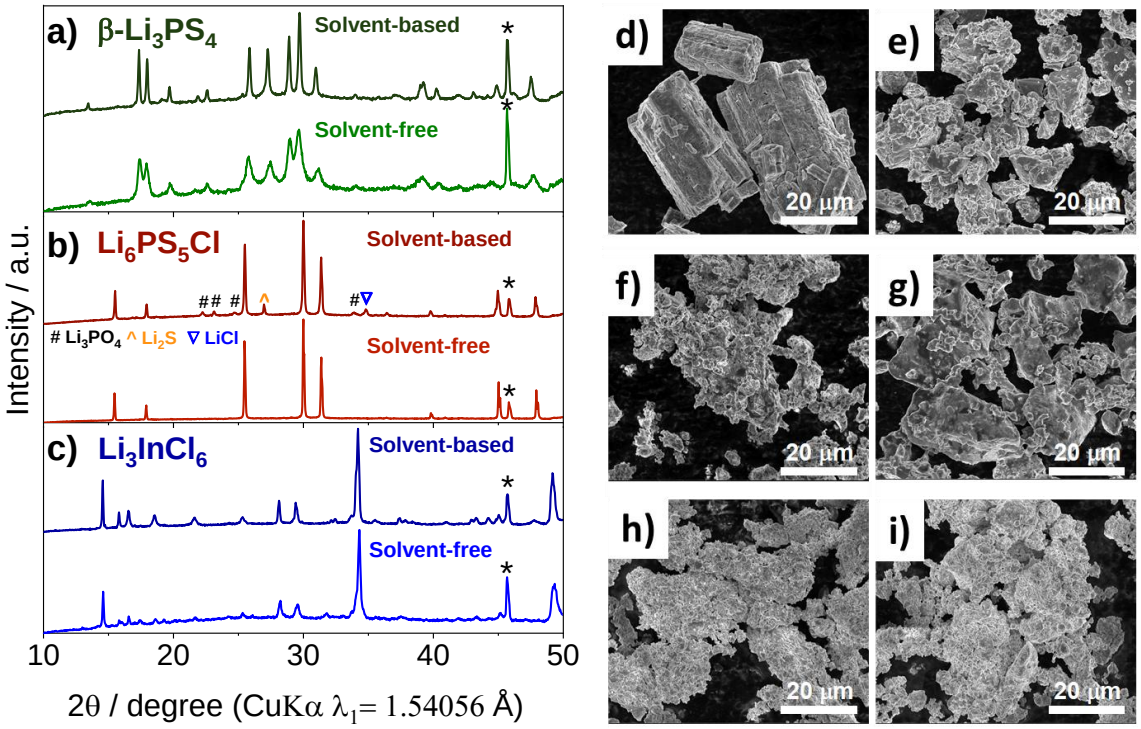

Figure 2: Powder X-ray diffraction patterns of a-c) W-β-Li_3PS_4 (dark green), C-β-Li_3PS_4 (green), W-Li_6PS_5Cl (wine), C-Li_6PS_5Cl (red), W-Li_3InCl_6 (navy) and C-Li_3InCl_6 (blue). Asterisks indicate Be reflections from the sample holder. SEM images of d) W-β-Li_3PS_4, e) C-β-Li_3PS_4, f) W-Li_6PS_5Cl, g) C-Li_6PS_5Cl, h) W-Li_3InCl_6 and i) C-Li_3InCl_6 as synthesized.

Room temperature ionic and electronic conductivities were determined for all the SEs by EIS and DC polarization (Figure S3), respectively, and are shown in Figure 3a and Figure 3b together with the corresponding EIS spectra in Figure 3c, d and e. A slightly better ionic conductivity was obtained for the solvent-free electrolytes compared to their counterpart prepared by wet route with the only exception of W-Li_3InCl_6. The obtained ionic conductivities rank as follows: Li_6PS_5Cl ($4x10^{-3}$ $S.cm^{-1}$), β-Li_3PS_4 ($0.66x10^{-3}$ $S.cm^{-1}$) and Li_3InCl_6, ($0.64x10^{-3}$ $S.cm^{-1}$) and are in line with previous reports.

Turning to the DC electronic conductivity, it remains nearly constant and equal to 10^{-9} - 10^{-10} S.cm^{-1} for most of SEs except for the W-Li_6PS_5Cl whose electronic conductivity is three orders of magnitude higher ($1.1x10^{-6}$ S.cm^{-1}) and exceed the values reported in the literature.[26] Interestingly, the DC electronic conductivity determined for the same W-Li_6PS_5Cl prior to the firing at 550°C was $1.8x10^{-9}$ S.cm^{-1} (Figure S3g). Thus, we believe that the enhanced electronic conductivity of W-Li_6PS_5Cl after firing could be rooted in the pyrolysis of residual solvent at high temperature (550 °C) yielding carbonaceous species. Overall, the highest ionic and lowest electronic conductivities were achieved by C-Li_6PS_5Cl and W-Li_3InCl_6 electrolytes.

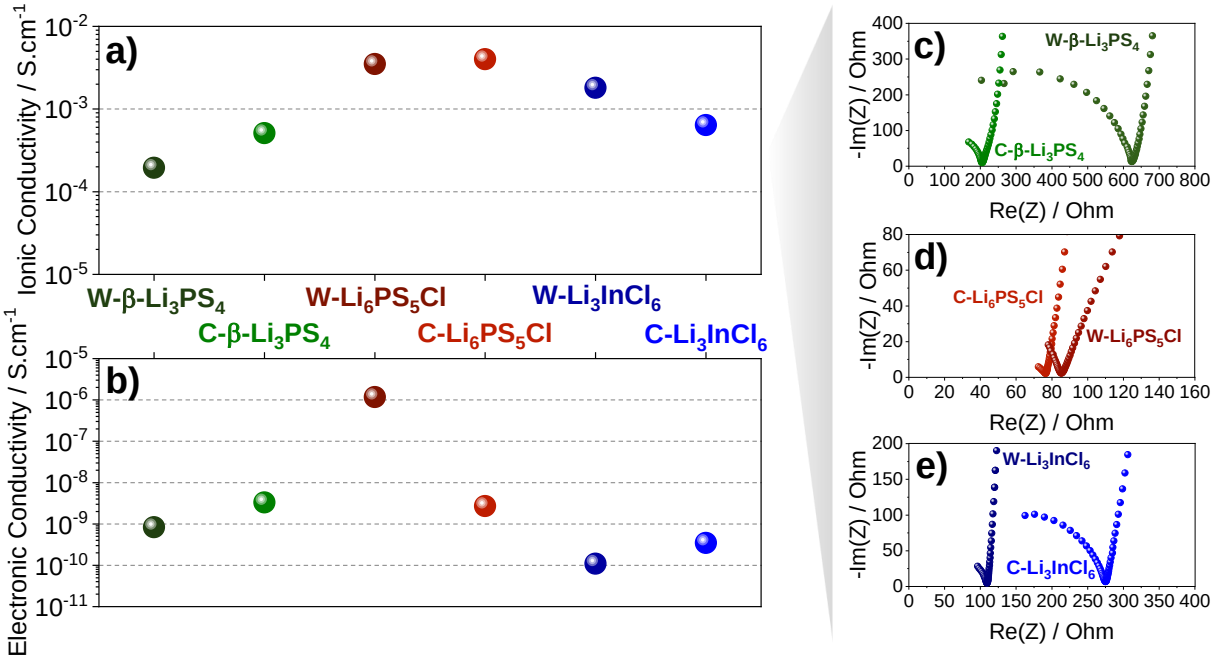

Figure 3: Comparison of a) ionic and b) electronic conductivities of studied solid electrolytes and Nyquist plots of c) β-Li_3PS_4, d) Li_6PS_5Cl and e) Li_3InCl_6 prepared through solvent-engineered and solvent-free methods.

Cathode composites and battery testing

Following the characterization of the pure solid electrolytes presented in the previous section, we proceeded to pair them with a high voltage cathode material and test the performance of the resulting composite in full ASSBs. To this effect, ASSBs containing the solid electrolytes under study were assembled and tested as described in the experimental section. A single positive electrode material coated-$LiNi_{0.6}Co_{0.2}Mn_{0.2}O_2$ (referred to as NMC622) was used throughout this work. In the case of β-Li_3PS_4 and Li_6PS_5Cl, the following

general configuration was used: coated-$LiNi_{0.6}Co_{0.2}Mn_{0.2}O_2$/**SE**/VGCF **|** **SE** **|** $Li_{0.5}In$/**SE**, where **SE** refers to the corresponding electrolyte. However, such configuration was not suitable to test Li_3InCl_6 due to its known instability at the anode interface leading to the reduction of In^{3+}.[34] Thus, a hetero-structure cell design was employed. It consists in the use of Li_3InCl_6 only in the cathode composite, C-Li_6PS_5Cl as separator and a composite made of C-Li_6PS_5Cl and $Li_{0.5}In$ as the anode. At least three cells were cycled for each cathode composite in order to assess reproducibility of the results.

Pairing coated-NMC622 with electrolytes obtained from solvent-free route (ceramic)

The voltage profiles of the first galvanostatic charge/discharge cycle as well as the evolution upon cycling of the discharge capacity are comparatively shown, respectively, in Figures 4a, 4b for the full-batteries containing electrolytes prepared by solvent-free route. Additionally, the cell polarization (ΔV, difference between average charge and discharge voltages as shown in Figure S4a) is depicted in Figure 4c.

The cell using coated-NMC622/C-Li_6PS_5Cl/VGCF composite positive electrode showed initial charge and discharge capacities of 173 and 141 mAh.g^{-1}, respectively (Figure 4a) with a 81.5% of Coulombic efficiency and a remarkable high capacity retention of 97% up to 20 cycles. (Figure 4b). With such figures of merits, C-Li_6PS_5Cl-based cells outpaces the ones containing C-Li_3InCl_6 and C-β-Li_3PS_4. In contrast, the analogous cell with a carbon-free cathode composite exhibited a limited initial capacity of 73 mAh.g^{-1}, which gradually increased up to 101 mAh.g^{-1} after 20 cycles (Figure S5a and 5b), most likely due to progressive activation of the CAM particles upon cycling. Additionally, such carbon-free batteries showed a higher cell resistance compared to their carbon-containing counterparts (Figure S6), in line with its poorer cycling performance. Overall, this indicates that the addition of carbon to the composite containing C-Li_6PS_5Cl enhanced the reversible capacity of the battery and its overall cycling performance without any major degradation (Figures 4c).

Turning to the cell based on carbon-containing coated-NMC622/C-β-Li_3PS_4 composite, it showed an initial charge and discharge capacities of 156 and 109 mAh.g^{-1}, respectively (Figure 4a) with a 10% capacity decay after 20 cycles (Figure 4b) as opposed to the carbon-free composite, which exhibited an almost constant discharge capacity of 110 mAh.g^{-1} (Figure S5b). Moreover, the carbon-containing composite showed an increase in polarization ΔV upon cycling (Figures 4c). In summary, the addition of carbon to β-Li_3PS_4-based composite electrodes resulted in a capacity boost but at expenses of a poor Coulombic efficiency and further capacity fading. Such a negative effect of carbon has been ascribed to its electron mediator role to trigger electrochemical-driven degradation.[35] The greater deterioration of β-Li_3PS_4 - carbon

composites rather than Li_6PS_5Cl - carbon ones is rooted in the lower stability against deterioration of the former at oxidation potentials greater than 3.2 V as deduced independently by EIS experiments.

Lastly, carbon-containing composite electrodes with C-Li_3InCl_6 (coated-NMC622/C-Li_3InCl_6) was tested using C-Li_6PS_5Cl as separator. High charge and discharge capacities were delivered in the first cycle (166 and 143 mAh.g^{-1}, respectively, Figure 4a), comparable to our best performing material (C-Li_6PS_5Cl-based composite). However, its capacity fading upon cycling resulted the worst of the three investigated systems, reaching 50% after 20 cycles (Figure 4b). Such a rapid capacity decay is mirrored by a fourfold increase of ΔV upon cycling (Figure 4c). Moreover, when replacing C-Li_6PS_5Cl testing separator by W-β-Li_3PS_4 separator, we observed an even greater capacity fade that reached 95% after cycling (Figure S7). In order to interrogate the origin of such a drastic capacity fading, we investigated the chemical compatibility between W-Li_3InCl_6 and the aforementioned electrolytes also used in the cell architecture. To this effect, C-Li_3InCl_6/C-Li_6PS_5Cl and C-Li_3InCl_6/W-β-Li_3PS_4 mixtures of the pristine powders (in 1:1 wt%) were prepared and subjected to a thermal treatment at 150°C during 72 hours in order to promote chemical reactivity. Thereafter, synchrotron X-ray powder diffraction of the annealed powders revealed the presence of LiCl as the decomposition product, thus confirming thermally promoted chemical reactions between the two solid electrolytes (Figure S8a and S8b). This degradation was certainly more pronounced in presence of β-Li_3PS_4, in consistence with the rapid performance degradation of halide-based cells using β-Li_3PS_4 as the separator. Bearing in mind that our heating treatment was below the synthesis temperature of the mother electrolytes (W-β-Li_3PS_4: 155 °C, C-Li_6PS_5Cl: 550 °C and C-Li_3InCl_6: 200 °C) and therefore far from their unstable thermal stability range, we can relate the newly found chemical instability of Li_3InCl_6 towards β-Li_3PS_4 and Li_6PS_5Cl to the cycling performance degradation of the hetero-structural battery. Such chemical incompatibility leads to the formation of a passivation interlayer between the positive electrode and the separator that is prejudicial to battery performances.

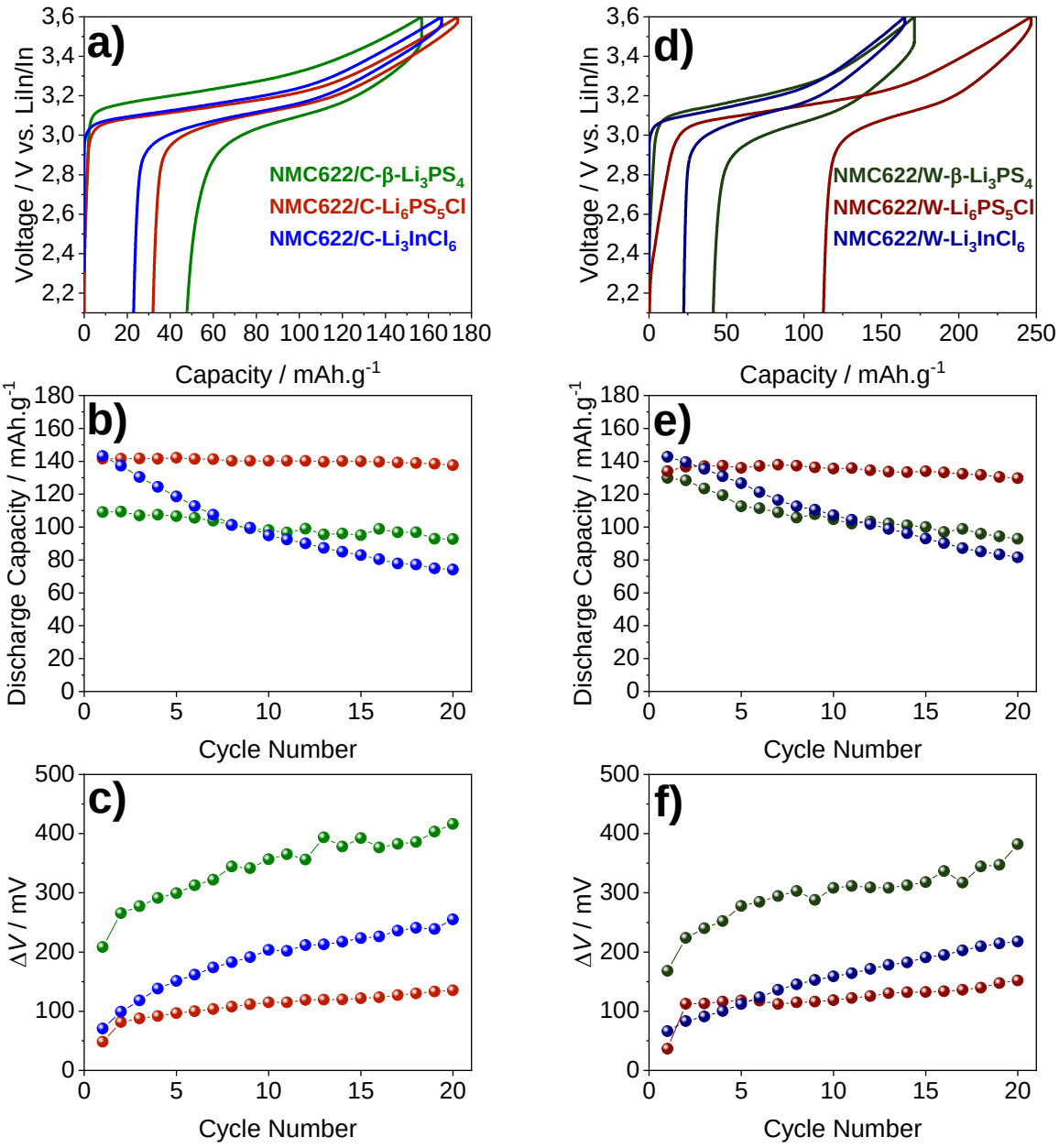

Figure 4: Electrochemical performance results of hand-ground carbon-containing coated-NMC622 and β-Li_3PS_4 / Li_6PS_5Cl / Li_3InCl_6 cathode composites in ASSBs at room temperature. Voltage profile of the first galvanostatic charge–discharge cycle, discharge capacity as a function of cycle number and cell polarization over cycling depicted, respectively, for the cells containing electrolytes prepared by solvent-free (a, b, c) and wet-based (d, e, f) synthesis routes.

Pairing coated-NMC622 with electrolytes obtained from wet route

The initial charge/discharge performances and the discharge capacity upon cycling are shown in Figures 4d and 4e respectively, for the full-batteries containing solid electrolytes synthesized by wet route. Additionally, the ΔV (the difference between average charge and discharge voltages as shown in Figure S4b) as a function of the cycle number is depicted in Figure 4f.

The cathode composite of the W-Li_6PS_5Cl (coated-NMC622/W-Li_6PS_5Cl/VGCF) exhibited a remarkably high first charge capacity of 246 mAh.g^{-1} accompanied by a pronounced oxidation slope starting at ~ 2.3 V, likely ascribed to electrolyte decomposition. In line with such hypothesis, the Coulombic efficiency of the first cycle was very poor (54.3%) (Figure 4d). This suggests a magnified electrochemical decomposition for the W-Li_6PS_5Cl, which may be possibly related to faster decomposition reaction[36] triggered by its unexpected very high electronic conductivity shown in the previous section together. Nevertheless, after completing the first cycle, the system showed a striking 96.8% of capacity retention and an almost constant Coulombic efficiency of 86.5% after 20 cycles (Figures 4e and S9, respectively). Note that, variation on fabrication conditions of W-Li_6PS_5Cl did not deliver better cycling performance (see Figure S10). Equally, the system showed a nearly stable ΔV and apparent resistance upon cycling represented in Figures 4f and S11, respectively. Interestingly, the carbon-free positive electrode displayed an increasing discharge capacity upon battery cycling starting from 67 mAh.g^{-1} up to 100 mAh.g^{-1} (Figure S5e), possibly related to a gradual activation of the CAM given along cycling, in the line with C-Li_6PS_5Cl reported above. Such an activation period upon cycling is nearly common to all the carbon-free positive electrodes. A possible reason could lie the repetitive contraction-expansion of the active material that enables through cycling a better contact between the active material and solid electrolyte, hence enabling a greater participation of the NMC particles and by the same token an increase in capacity.

When moving to the W-β-Li_3PS_4, carbon-containing composite (coated-NMC622/W-β-Li_3PS_4) exhibited a relatively high charge and discharge capacities upon the first cycle (171 and 129 mAh.g^{-1}, respectively) that is accompanied by a rapid capacity decay of 71.5% after 20 cycles. This differs from the analogous carbon-free composite, which delivered a stable discharge capacity of 58 mAh.g^{-1} upon cycling (Figures S5d and S5e). The differences between the carbon-containing and carbon-free composites are also reflected in the evolution of the cell polarization (ΔV) which either increases (Figure 4f) or remains constant (Figure S5f) upon cycling, respectively. We believe that such a carbon-driven decrease in performance is nested in the electrochemical degradation of the solid electrolyte that is evidenced as a sloping region at the early stage of the first charge (~2.3V), in line with the reported study in literature.[37] Aside from such detrimental effects, a beneficial effect of carbon is that it enables to tap more capacity from the positive composite electrode via improved electronic conductivity as already well-described.[37–39]

Lastly, we tested W-Li_3InCl_6 in a dual solid electrolyte cell architecture, as described above. A first charge and discharge capacities of 165 and 142 $mAh.g^{-1}$ respectively (Figure 4d) was obtained together with the lowest irreversible capacity through the first cycle (13.6%) obtained among all the cathode-solid ionic conductor pairs tested in this work. However, a progressive capacity degradation was observed, reaching a 50% of decay after 20 cycles (Figure 4e) as witnessed by an increase in ΔV (Figures 4f), analogous to the case of C-Li_3InCl_6 reported above. As it was previously shown, the scenario upon cycling became worse when switching to W-β-Li_3PS_4 as separator, with a rapid capacity decay (11.7% after 20 cycles) (Figure S12). To further evaluate the origin of the electrochemical degradation in the dual solid electrolyte cell structure, W-Li_3InCl_6-based cathode composite was tested in a three-electrode cell configuration using C-Li_6PS_5Cl as separator and $Li_{0.5}In$/C-Li_6PS_5Cl as reference and negative electrode. Galvanostatic cycling together with EIS measurements were performed in order to monitor the impedance evolution upon cycling of the positive and negative electrode separately (see experimental details). Figure 5a displayed the comparison of galvanostatic cycling profiles of positive and negative electrodes between first and 20^{th} cycles, which exhibit a pronounced capacity degradation, consistent with the two-electrode cell setup, as well as higher polarization in positive electrode rather than negative electrode after 20 cycles. On the other hand, the impedance response revealed that the most significant change came from the positive electrode by delivering up to a six-fold increase of the resistance at f= 1Hz after 20 cycles (Figure 5b). Such impedance response was mainly originated in the mid frequency region as opposed to the high frequency region. In contrast to the remarkable impedance growth at the positive electrode interface, no significant impedance enhancement was observed for the negative electrode over cycling (Figure 5c). When reconstructing the hetero-structure with W-β-Li_3PS_4 as separator, the impedance increase in the positive electrode became even higher over cycling, aligned with its rapid electrochemical cell fading (Figure S13). Overall, the electrochemical performance degradation in the hetero-structure cell of W-Li_3InCl_6-based cathode composite upon cycling was found via three-electrode cell-setup to originate from highly resistive positive electrode interface. This interfacial resistance as well as the poor performances of halide-based cells are rooted in the chemical incompatibility between Li_3InCl_6 towards the two sulfide-based electrolytes used in the heterogeneous cell architecture, evidenced in their thermally driven reactivity at low temperature as shown in Figure S14a and b.

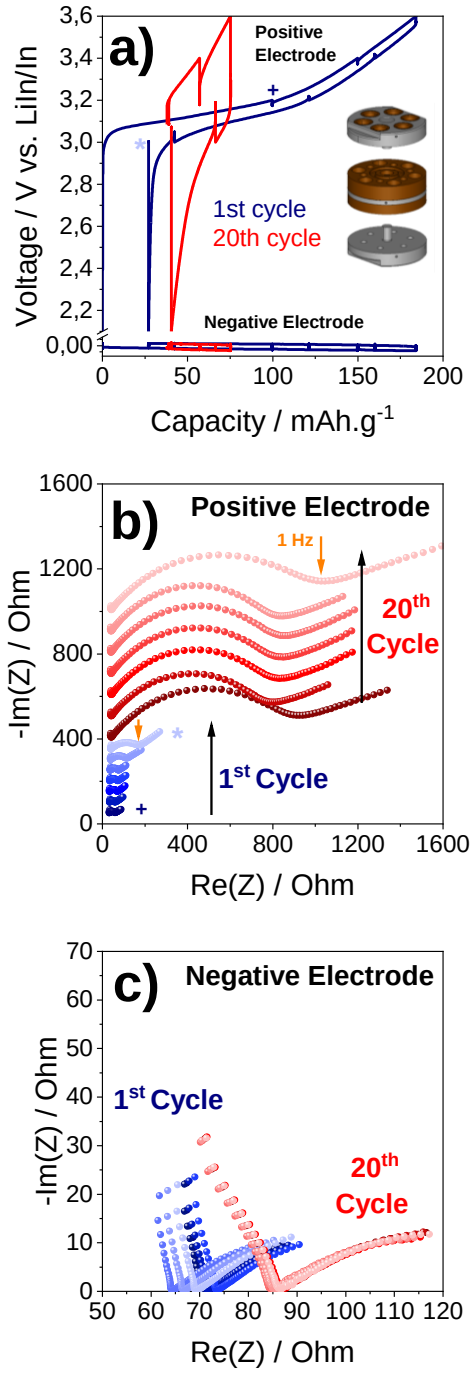

Figure 5: Galvanostatic voltage profiles of W-Li_3InCl_6/coated-NMC622/VGCF positive electrode, C-Li_6PS_5Cl as separator and $Li_{0.5}In$/C-Li_6PS_5Cl negative electrode in three-electrode cell configuration a) 1st and 20th cycle curves. The impedance spectrums of b) the W-Li_3InCl_6/coated-NMC622/VGCF positive electrode, where the symbols show first and last impedance sequence over cycle and the black arrows indicate the evolution of the impedance at each cycle (offset was added between each impedance spectrums) and c) the $Li_{0.5}In$/C-Li_6PS_5Cl negative electrode for each charge and discharge sequences for 1st and 20th cycles.

Pairing coated-NMC622 with solvent-based electrolytes in a core-shell architecture

Inspired by earlier literature reports, we have replaced our hand grinding-based procedure for cathode composite preparation by a process consisting in seeding our reacting electrolyte solution in presence of cathode active material powders (coated-NMC622). The idea behind such new strategy is to produce cathode particles coated with SE in a core-shell like structure and thus to favor the intimate contact between these two components. However, such an implementation was not free of complications. Synthesis limitations became quickly evident for the argyrodite-based and halide-based composites, namely during the subsequent temperature treatment of the solution. For instance, we experienced a structural degradation of W-Li_6PS_5Cl-coated NMC622 powders when firing at 550 °C as shown by XRD (Figure S15). We thus limited the annealing temperature to 155 °C thus sacrifying the SE ionic conductivity which reaches its maximum ($3.5x10^{-3}$ $S.cm^{-1}$) for W-Li_6PS_5Cl powders fired at 550 °C. Moving to halides did not simplify the task since re-crystallized W-Li_3InCl_6 from THF solution at 200 °C in either absence or presence of coated-NMC622 particles revealed a multi-phased product as evidenced by XRD (Figure S16a) that has an order of magnitude lower ionic conductivity (Figure S16b). In contrast, W-β-Li_3PS_4-coated NMC622 based composites could be successfully prepared at 155 °C via our solution process without any major roadblock.

Figures 6a-c show SEM micrographs and EDX analysis for the prepared composites based on W-β-Li_3PS_4, W-Li_6PS_5Cl and W-Li_3InCl_6. In all cases, the rounded rather than salient particle edges pertaining to coated-NMC622 suggest the presence of deposits. However, they differ in their EDX mapping indicating a uniform repartition of Ni and P for the W-β-Li_3PS_4-coated NMC622 particles as opposed to a non-uniform repartition for the two other composites (see Cl and In mapping on Figure 6b and 6c, respectively), hence confirming the difficulties in achieving efficient core-shell coated particles.

Despite these differences, the cycling performance of the composites were tested in full ASSBs assembled within the same electrode-electrolyte configuration and results are solely reported after duplicated measurements. The results are recapped in Figures 6d-f, respectively. The composite based on W-Li_3InCl_6 showed the worst performance, and this does not come as a surprise in light of phase purity and non-uniform deposit issues deduced from combined XRD and conductivity results. Similar but less pronounced problems rendered the performance of W-Li_6PS_5Cl-coated composites, which resulted worse capacity than those obtained previously on hand-ground Li_6PS_5Cl-based cathode composites. Turning to the performance of W-β-Li_3PS_4-coated NMC622 cathode composite, it nearly compares to that of their hand-ground counterpart with in one way a lower reversible capacity (118 vs. 129 $mAh.g^{-1}$) but a slightly higher capacity retention after 20 cycles (78% vs. 75.8%). It is worth mentioning that adding carbon additives to this composite electrode resulted in a deterioration of the capacity retention, in line of what observed before (Figure S17). Altogether, these results provide no advantage of the in-situ solution coating of coated-

NMC622 particles by SEs. Other approaches towards the synthesis of tailor made core-shell particles remains to be developed.

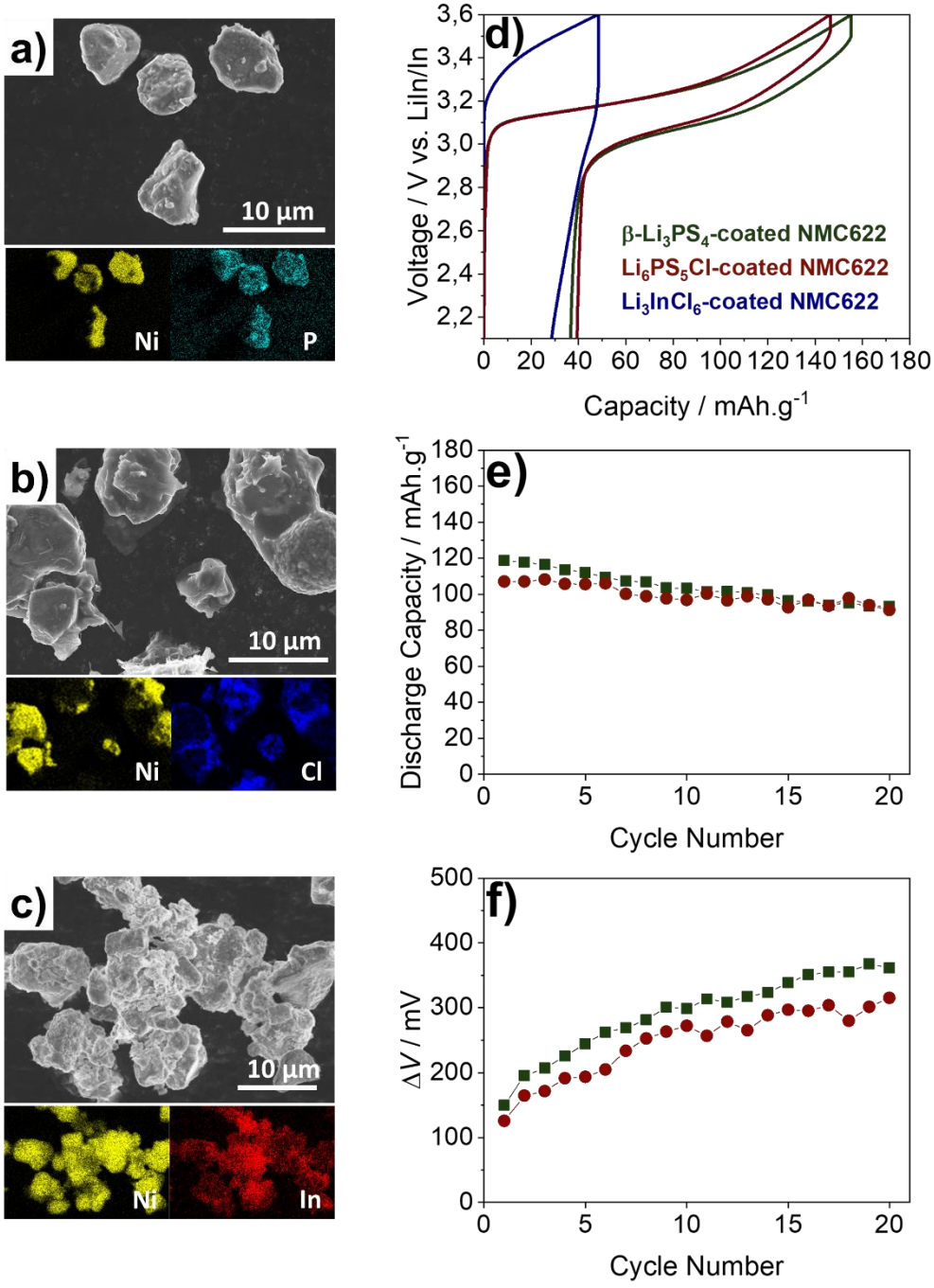

Figure 6: SEM images and the corresponding EDX elemental maps (representative elements nickel, phosphorous, chlorine and indium are shown in yellow, turquoise, blue and red for coated-NMC622, W-β-Li_3PS_4, W-Li_6PS_5Cl and W-Li_3InCl_6, respectively) of a) W-β-Li_3PS_4-coated NMC622, b) W-Li_6PS_5Cl-

coated NMC622 and c) W-Li_3InCl_6-coated NMC622 powders as synthesized, where the solid electrolytes are witnessed as a shell onto the coated-NMC622 core particles. Electrochemical performance results of β-Li_3PS_4-coated NMC622, W-Li_6PS_5Cl-coated NMC622 and W-Li_3InCl_6-coated NMC622 carbon-containing cathode composites in ASSBs at C/20 between 2.1 V and 3.6 V vs. In/InLi at room temperature d) first cycle charge–discharge capacity curves, e) the discharge capacity versus cycle number and f) cell polarization upon cycling.

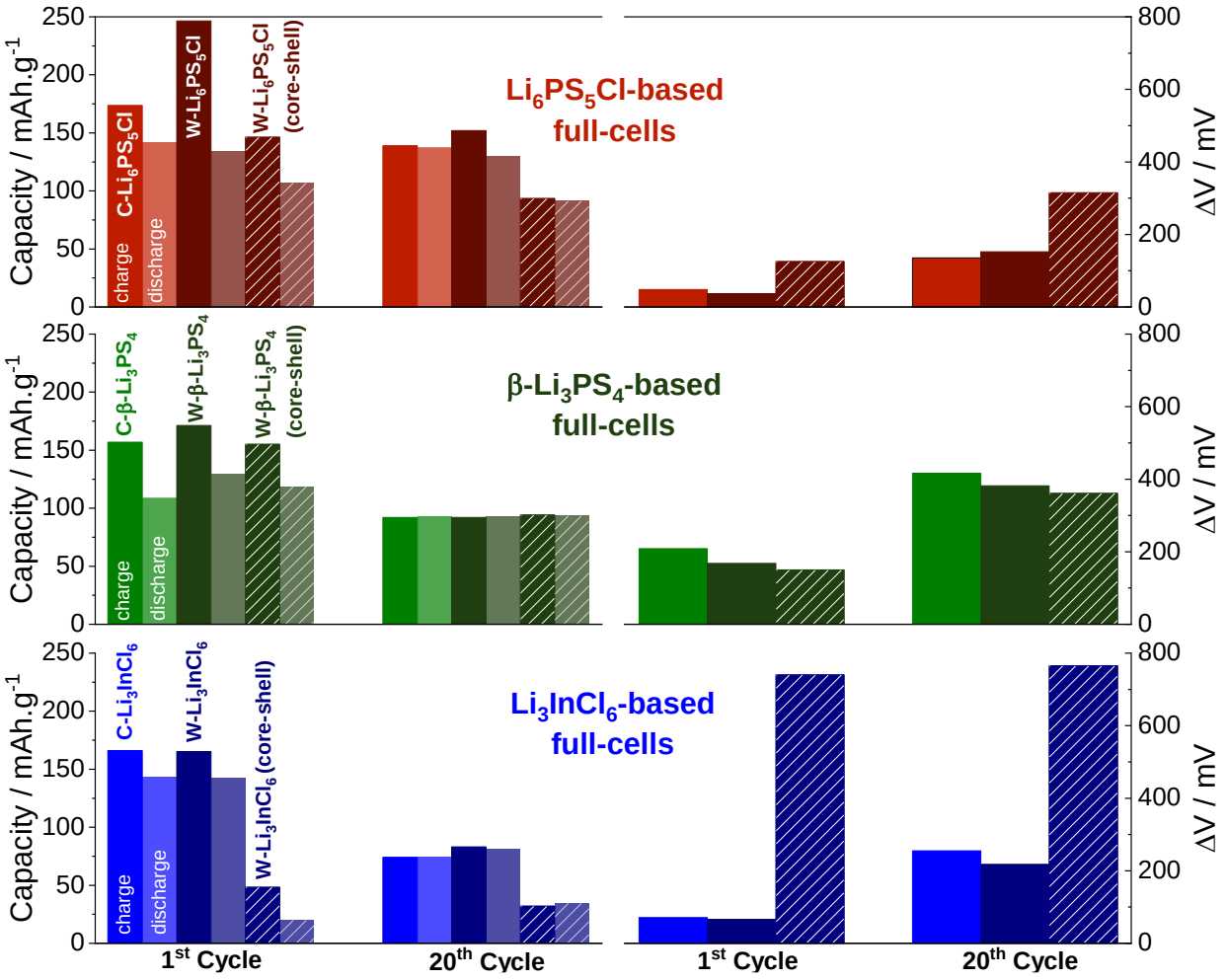

Figure 7: Comparison of the charge (dark colored bars) - discharge (light colored bars) capacities and the cell polarization of the all studied carbon-based cathode composites between 1st and 20th cycles.

Conclusion

We have herein reported systematic crossed-comparisons of the chemical/electrochemical compatibility of coated-$LiNi_{0.6}Mn_{0.2}Co_{0.2}O_2$ cathode material against the today's three most studied solid ionic conductors prepared via various synthesis approaches. From this survey, which has not taken into accounts effects of particle size and morphology, we found that solvent-free synthesis leads to high ionic and low electronic conduction, impurity-free structure and high densification for solid ionic conductors (except for Li_3InCl_6). Furthermore, amongst all studied cathode composites whose electrochemical performance results are recapped in Figure 7, C-Li_6PS_5Cl and coated-$LiNi_{0.6}Mn_{0.2}Co_{0.2}O_2$ composite positive electrode (hand-ground) was found to enable the best electrochemical cycling performance with a sustained reversible capacity of 141 $mAh.g^{-1}$ for at least 20 cycles in all-solid-state batteries and preserved the best performance upon 50 cycles as shown in Figure S18. This remarkable performance was linked to the presence of carbon additive to boost the electronic conductivity of cathode composite at expenses of its detrimental effect on sulfide-based solid ionic conductors, as we obtained in β-Li_3PS_4-based cathode composites with capacity degradation up to 30%. This illustrates two sides of the same coin when considering how adding carbon in the cathode composite will affect the battery performance. Whereas a boost in the electronic conduction of the cathode may be beneficial capacity-wise, it can also promote electrolyte decomposition as deduced from XRD measurements, which will translate into poor Coulombic efficiency and capacity fading. The extent of this decomposition depends upon the thermodynamic stability of the ionic conductor with respect to the active material for which DFT can inform us. A way to alleviate such deterioration of the SE is to use sulfide-based composite electrodes such as $Li_{1.13}Ti_{0.57}Fe_{0.33}S_2$ rather than oxide ones (NMC) which operating voltage falls within the range of the electrolyte stability so that coatings are not needed. Sulfides offers better ionic and electronic conductivities, both leading to a smaller polarization with however a penalty in terms of energy density owing to their lower redox voltage as compared to oxides.

Through this study, we have revealed the limitations of solvent-assisted synthesis approach of solid electrolytes, namely residual solvent and phase purity issues, which perturb both chemical and electrochemical properties. Although conceptually elegant, the in-situ design of core-shell cathode active material-solid electrolyte structures in solution was shown to suffer from detrimental effect of solvents on solid electrolytes or chemical instability between layered oxide and sulfide-based solid electrolyte at high temperature, hence they observed limited performances compared to hand-ground cathode composites.

Halide-based solid electrolytes are particularly attractive for their high voltage stability and therefore for its electrochemical compatibility with oxide-based cathode materials. However, their instability towards Li-based anodes rules out the possibility of having full halide-based cell architectures. To contour this

difficulty, specific cell configurations with either β-Li_3PS_4 or Li_6PS_5Cl interposed between the halide positive composite electrode and the negative were used. While enabling to quantify the performances of ASSBs based on halide-based composite electrode, our study has clearly revealed, via combined synchrotron-XRD and impedance measurements, the chemical incompatibility between Li_3InCl_6 and either Li_6PS_5Cl or β-Li_3PS_4 that translates into the formation of a passivation interlayer in the hetero-structure cell design, which leads to degraded electrochemical performance up to 50% upon cycling. Obviously, the presence of a triple phase NMC-Li_6PS_5Cl-Li_3InCl_6 contact point within a composite is detrimental. Thus, designing hetero-structured separators together with anodic protective approaches stands as common strategies to overcome these interface issues. They are being explored in our group and preliminary data indicate promising results, hence enabling to envision the future use of halides in solid-state batteries.

Overall, we hope this work could provide guidance in properly selecting optimized electrolyte-electrode pairs for developing practical all-solid-state batteries.

Associated Content

Supporting Information

Rietveld refinement of the XRD pattern of W-Li_6PS_5Cl, comparison of relative density for β-Li_3PS_4, Li_6PS_5Cl and Li_3InCl_6 (prepared via dry and wet synthesis methods), DC polarization curves of β-Li_3PS_4, Li_6PS_5Cl and Li_3InCl_6 (synthesized by solvent-based and solvent-free routes), average charge and discharge profiles of cathode composites containing carbon additive, electrochemical performance results of carbon-free cathode composites, evolution of apparent resistance over cycling for the cathode composites with solid electrolytes prepared by dry route, galvanostatic cycling performance of coated-NMC622/C-Li_3InCl_6/VGCF | W-β-Li_3PS_4 | $Li_{0.5}In$/W-β-Li_3PS_4 solid-state hetero-structure battery, Rietveld refinement of the SXRD patterns for mixtures of C-Li_3InCl_6 - C-Li_6PS_5Cl and C-Li_3InCl_6 - W-β-Li_3PS_4 after thermal treatment, Coulombic efficiency of coated-NMC622/W-Li_6PS_5Cl/VGCF | W-Li_6PS_5Cl | $Li_{0.5}In$/W-Li_6PS_5Cl solid-state battery over cycling, apparent resistance of the cathode composites containing solvent-mediated solid electrolytes, electrochemical cycling performance of coated-NMC622/W-Li_3InCl_6/VGCF | W-β-Li_3PS_4 | $Li_{0.5}In$/W-β-Li_3PS_4 solid-state hetero-structure battery, W-Li_3InCl_6/coated-NMC622/VGCF | W-β-Li_3PS_4 | $Li_{0.5}In$/W-β-Li_3PS_4 solid-state battery of electrochemical characterizations(galvanostatic and EIS) in three-electrode cell setup, Rietveld refinement of the SXRD patterns for thermally promoted mixtures of W-Li_3InCl_6 - C-Li_6PS_5Cl and W-Li_3InCl_6 - W-β-Li_3PS_4, XRD patterns of the W-Li_6PS_5Cl-based cathode composite (core-shell architecture), characterization(XRD and EIS) of Li_3InCl_6 exposed to THF,

galvanostatic cycling result of W-β-Li_3PS_4-coated NMC622 (coated) cathode composite (core-shell process) in carbon-free system, electrochemical performance results of carbon-containing cathode composites over 50 cycles.

Notes

The authors declare no competing financial interest.

Acknowledgements

The authors thank Bernhard Leube for fruitful discussions on argyrodite synthesis, Marie-Francine Lagadec for EDX imaging, Biao Li and Parth Desai for helpful discussions. We acknowledge the precious help of Benoît Baptiste (IMPMC, Sorbonne Université) who collected the SXRD patterns at the CRISTAL beamline of Synchrotron Soleil (BAG proposal number 20201440); staff from SOLEIL is also acknowledged.

References

(1) Kamaya, N.; Homma, K.; Yamakawa, Y.; Hirayama, M.; Kanno, R.; Yonemura, M.; Kamiyama, T.; Kato, Y.; Hama, S.; Kawamoto, K.; Mitsui, A. A Lithium Superionic Conductor. *Nature Mater* **2011**, *10* (9), 682–686. https://doi.org/10.1038/nmat3066.

(2) Janek, J.; Zeier, W. G. A Solid Future for Battery Development. *Nat Energy* **2016**, *1* (9), 16141. https://doi.org/10.1038/nenergy.2016.141.

(3) Banerjee, A.; Wang, X.; Fang, C.; Wu, E. A.; Meng, Y. S. Interfaces and Interphases in All-Solid-State Batteries with Inorganic Solid Electrolytes. *Chem. Rev.* **2020**, *120* (14), 6878–6933. https://doi.org/10.1021/acs.chemrev.0c00101.

(4) Marchini, F.; Saha, S.; Alves Dalla Corte, D.; Tarascon, J. M. Li-Rich Layered Sulfide as Cathode Active Materials in All-Solid-State Li–Metal Batteries. *ACS Appl. Mater. Interfaces* **2020**, *12* (13), 15145–15154. https://doi.org/10.1021/acsami.9b22937.

(5) Famprikis, T.; Canepa, P.; Dawson, J. A.; Islam, M. S.; Masquelier, C. Fundamentals of Inorganic Solid-State Electrolytes for Batteries. *Nat. Mater.* **2019**, *18* (12), 1278–1291. https://doi.org/10.1038/s41563-019-0431-3.

(6) Yan, K.; Lu, Z.; Lee, H.-W.; Xiong, F.; Hsu, P.-C.; Li, Y.; Zhao, J.; Chu, S.; Cui, Y. Selective Deposition and Stable Encapsulation of Lithium through Heterogeneous Seeded Growth. *Nat Energy* **2016**, *1* (3), 16010. https://doi.org/10.1038/nenergy.2016.10.

(7) Lee, Y.-G.; Fujiki, S.; Jung, C.; Suzuki, N.; Yashiro, N.; Omoda, R.; Ko, D.-S.; Shiratsuchi, T.; Sugimoto, T.; Ryu, S.; Ku, J. H.; Watanabe, T.; Park, Y.; Aihara, Y.; Im, D.; Han, I. T. High-Energy Long-Cycling All-Solid-State Lithium Metal Batteries Enabled by Silver–Carbon Composite Anodes. *Nat Energy* **2020**, *5* (4), 299–308. https://doi.org/10.1038/s41560-020-0575-z.

(8) Zhang, W.; Weber, D. A.; Weigand, H.; Arlt, T.; Manke, I.; Schröder, D.; Koerver, R.; Leichtweiss, T.; Hartmann, P.; Zeier, W. G.; Janek, J. Interfacial Processes and Influence of Composite Cathode Microstructure Controlling the Performance of All-Solid-State Lithium Batteries. *ACS Appl. Mater. Interfaces* **2017**, *9* (21), 17835–17845. https://doi.org/10.1021/acsami.7b01137.

(9) Strauss, F.; Stepien, D.; Maibach, J.; Pfaffmann, L.; Indris, S.; Hartmann, P.; Brezesinski, T. Influence of Electronically Conductive Additives on the Cycling Performance of Argyrodite-Based All-Solid-State Batteries. *RSC Adv.* **2020**, *10* (2), 1114–1119. https://doi.org/10.1039/C9RA10253A.

(10) Walther, F.; Koerver, R.; Fuchs, T.; Ohno, S.; Sann, J.; Rohnke, M.; Zeier, W. G.; Janek, J. Visualization of the Interfacial Decomposition of Composite Cathodes in Argyrodite-Based All-Solid-State Batteries Using Time-of-Flight Secondary-Ion Mass Spectrometry. *Chem. Mater.* **2019**, *31* (10), 3745–3755. https://doi.org/10.1021/acs.chemmater.9b00770.

(11) Tan, D. H. S.; Wu, E. A.; Nguyen, H.; Chen, Z.; Marple, M. A. T.; Doux, J.-M.; Wang, X.; Yang, H.; Banerjee, A.; Meng, Y. S. Elucidating Reversible Electrochemical Redox of Li_6PS_5Cl Solid Electrolyte. *ACS Energy Lett.* **2019**, *4* (10), 2418–2427. https://doi.org/10.1021/acsenergylett.9b01693.

(12) Xiao, Y.; Miara, L. J.; Wang, Y.; Ceder, G. Computational Screening of Cathode Coatings for Solid-State Batteries. *Joule* **2019**, *3* (5), 1252–1275. https://doi.org/10.1016/j.joule.2019.02.006.

(13) Culver, S. P.; Koerver, R.; Zeier, W. G.; Janek, J. On the Functionality of Coatings for Cathode Active Materials in Thiophosphate-Based All-Solid-State Batteries. *Adv. Energy Mater.* **2019**, *9* (24), 1900626. https://doi.org/10.1002/aenm.201900626.

(14) Strauss, F.; Teo, J. H.; Maibach, J.; Kim, A.-Y.; Mazilkin, A.; Janek, J.; Brezesinski, T. Li_2ZrO_3-Coated NCM622 for Application in Inorganic Solid-State Batteries: Role of Surface Carbonates in the Cycling Performance. *ACS Appl. Mater. Interfaces* **2020**, *12* (51), 57146–57154. https://doi.org/10.1021/acsami.0c18590.

(15) Kato, Y.; Hori, S.; Kanno, R. Li $_{10}$ GeP $_{2}$ S $_{12}$ -Type Superionic Conductors: Synthesis, Structure, and Ionic Transportation. *Adv. Energy Mater.* **2020**, *10* (42), 2002153. https://doi.org/10.1002/aenm.202002153.

(16) Li, X.; Liang, J.; Yang, X.; Adair, K. R.; Wang, C.; Zhao, F.; Sun, X. Progress and Perspectives on Halide Lithium Conductors for All-Solid-State Lithium Batteries. *Energy Environ. Sci.* **2020**, *13* (5), 1429–1461. https://doi.org/10.1039/C9EE03828K.

(17) Park, D.; Park, H.; Lee, Y.; Kim, S.-O.; Jung, H.-G.; Chung, K. Y.; Shim, J. H.; Yu, S. Theoretical Design of Lithium Chloride Superionic Conductors for All-Solid-State High-Voltage Lithium-Ion Batteries. *ACS Appl. Mater. Interfaces* **2020**, *12* (31), 34806–34814. https://doi.org/10.1021/acsami.0c07003.

(18) Li, X.; Liang, J.; Chen, N.; Luo, J.; Adair, K. R.; Wang, C.; Banis, M. N.; Sham, T.; Zhang, L.; Zhao, S.; Lu, S.; Huang, H.; Li, R.; Sun, X. Water-Mediated Synthesis of a Superionic Halide Solid Electrolyte. *Angew. Chem. Int. Ed.* **2019**, *58* (46), 16427–16432. https://doi.org/10.1002/anie.201909805.

(19) Zhang, S.; Zhao, F.; Wang, S.; Liang, J.; Wang, J.; Wang, C.; Zhang, H.; Adair, K.; Li, W.; Li, M.; Duan, H.; Zhao, Y.; Yu, R.; Li, R.; Huang, H.; Zhang, L.; Zhao, S.; Lu, S.; Sham, T.; Mo, Y.; Sun, X. Advanced High-Voltage All-Solid-State Li-Ion Batteries Enabled by a Dual-Halogen Solid Electrolyte. *Adv. Energy Mater.* **2021**, 2100836. https://doi.org/10.1002/aenm.202100836.

(20) Zhou, L.; Kwok, C. Y.; Shyamsunder, A.; Zhang, Q.; Wu, X.; Nazar, L. F. A New Halospinel Superionic Conductor for High-Voltage All Solid State Lithium Batteries. *Energy Environ. Sci.* **2020**, *13* (7), 2056–2063. https://doi.org/10.1039/D0EE01017K.

(21) Liang, J.; Li, X.; Wang, S.; Adair, K. R.; Li, W.; Zhao, Y.; Wang, C.; Hu, Y.; Zhang, L.; Zhao, S.; Lu, S.; Huang, H.; Li, R.; Mo, Y.; Sun, X. Site-Occupation-Tuned Superionic Li $_{x}$ ScCl $_{3+x}$ Halide Solid Electrolytes for All-Solid-State Batteries. *J. Am. Chem. Soc.* **2020**, *142* (15), 7012–7022. https://doi.org/10.1021/jacs.0c00134.

(22) Kim, K.; Park, D.; Jung, H.-G.; Chung, K. Y.; Shim, J. H.; Wood, B. C.; Yu, S. Material Design Strategy for Halide Solid Electrolytes Li $_{3}$ MX $_{6}$ (X = Cl, Br, and I) for All-Solid-State High-Voltage Li-Ion Batteries. *Chem. Mater.* **2021**, *33* (10), 3669–3677. https://doi.org/10.1021/acs.chemmater.1c00555.

(23) Kudu, Ö. U.; Famprikis, T.; Fleutot, B.; Braida, M.-D.; Le Mercier, T.; Islam, M. S.; Masquelier, C. A Review of Structural Properties and Synthesis Methods of Solid Electrolyte Materials in the Li2S − P2S5 Binary System. *Journal of Power Sources* **2018**, *407*, 31–43. https://doi.org/10.1016/j.jpowsour.2018.10.037.

(24) Ghidiu, M.; Ruhl, J.; Culver, S. P.; Zeier, W. G. Solution-Based Synthesis of Lithium Thiophosphate Superionic Conductors for Solid-State Batteries: A Chemistry Perspective. *J. Mater. Chem. A* **2019**, *7* (30), 17735–17753. https://doi.org/10.1039/C9TA04772G.

(25) Schlem, R.; Burmeister, C. F.; Michalowski, P.; Ohno, S.; Dewald, G. F.; Kwade, A.; Zeier, W. G. Energy Storage Materials for Solid-State Batteries: Design by Mechanochemistry. *Adv. Energy Mater.* **2021**, 2101022. https://doi.org/10.1002/aenm.202101022.

(26) Zhou, L.; Park, K.-H.; Sun, X.; Lalère, F.; Adermann, T.; Hartmann, P.; Nazar, L. F. Solvent-Engineered Design of Argyrodite Li_6PS_5X (X = Cl, Br, I) Solid Electrolytes with High Ionic Conductivity. *ACS Energy Lett.* **2019**, *4* (1), 265–270. https://doi.org/10.1021/acsenergylett.8b01997.

(27) Wang, C.; Liang, J.; Jiang, M.; Li, X.; Mukherjee, S.; Adair, K.; Zheng, M.; Zhao, Y.; Zhao, F.; Zhang, S.; Li, R.; Huang, H.; Zhao, S.; Zhang, L.; Lu, S.; Singh, C. V.; Sun, X. Interface-Assisted in-Situ Growth of Halide Electrolytes Eliminating Interfacial Challenges of All-Inorganic Solid-State Batteries. *Nano Energy* **2020**, *76*, 105015. https://doi.org/10.1016/j.nanoen.2020.105015.

(28) Yubuchi, S.; Uematsu, M.; Deguchi, M.; Hayashi, A.; Tatsumisago, M. Lithium-Ion-Conducting Argyrodite-Type Li_6PS_5X (X = Cl, Br, I) Solid Electrolytes Prepared by a Liquid-Phase Technique Using Ethanol as a Solvent. *ACS Appl. Energy Mater.* **2018**, *1* (8), 3622–3629. https://doi.org/10.1021/acsaem.8b00280.

(29) Park, K. H.; Oh, D. Y.; Choi, Y. E.; Nam, Y. J.; Han, L.; Kim, J.-Y.; Xin, H.; Lin, F.; Oh, S. M.; Jung, Y. S. Solution-Processable Glass LiI-Li_4SnS_4 Superionic Conductors for All-Solid-State Li-Ion Batteries. *Adv. Mater.* **2016**, *28* (9), 1874–1883. https://doi.org/10.1002/adma.201505008.

(30) Marchini, F.; Porcheron, B.; Rousse, G.; Albero Blanquer, L.; Droguet, L.; Foix, D.; Koç, T.; Deschamps, M.; Tarascon, J. M. The Hidden Side of Nanoporous B-Li_3PS_4 Solid Electrolyte. *Adv. Energy Mater.* **2021**, *11* (34), 2101111. https://doi.org/10.1002/aenm.202101111.

(31) Ruhl, J.; Riegger, L. M.; Ghidiu, M.; Zeier, W. G. Impact of Solvent Treatment of the Superionic Argyrodite Li_6PS_5Cl on Solid-State Battery Performance. *Adv Energy Sustain Res* **2021**, *2* (2), 2000077. https://doi.org/10.1002/aesr.202000077.

(32) Han, Y.; Jung, S. H.; Kwak, H.; Jun, S.; Kwak, H. H.; Lee, J. H.; Hong, S.; Jung, Y. S. Single- or Poly-Crystalline Ni-Rich Layered Cathode, Sulfide or Halide Solid Electrolyte: Which Will Be the Winners for All-Solid-State Batteries? *Adv. Energy Mater.* **2021**, *11* (21), 2100126. https://doi.org/10.1002/aenm.202100126.

(33) Dugas, R.; Dupraz, Y.; Quemin, E.; Koç, T.; Tarascon, J.-M. Engineered Three-Electrode Cells for Improving Solid State Batteries. *J. Electrochem. Soc.* **2021**, *168* (9), 090508. https://doi.org/10.1149/1945-7111/ac208d.

(34) Riegger, L. M.; Schlem, R.; Sann, J.; Zeier, W. G.; Janek, J. Lithium-Metal Anode Instability of the Superionic Halide Solid Electrolytes and the Implications for Solid-State Batteries. *Angew. Chem. Int. Ed.* **2021**, *60* (12), 6718–6723. https://doi.org/10.1002/anie.202015238.

(35) Li, M.; Bai, Z.; Li, Y.; Ma, L.; Dai, A.; Wang, X.; Luo, D.; Wu, T.; Liu, P.; Yang, L.; Amine, K.; Chen, Z.; Lu, J. Electrochemically Primed Functional Redox Mediator Generator from the Decomposition of Solid State Electrolyte. *Nat Commun* **2019**, *10* (1), 1890. https://doi.org/10.1038/s41467-019-09638-4.

(36) Nakamura, T.; Amezawa, K.; Kulisch, J.; Zeier, W. G.; Janek, J. Guidelines for All-Solid-State Battery Design and Electrode Buffer Layers Based on Chemical Potential Profile Calculation. *ACS Appl. Mater. Interfaces* **2019**, *11* (22), 19968–19976. https://doi.org/10.1021/acsami.9b03053.

(37) Tan, D. H. S.; Banerjee, A.; Chen, Z.; Meng, Y. S. From Nanoscale Interface Characterization to Sustainable Energy Storage Using All-Solid-State Batteries. *Nat. Nanotechnol.* **2020**, *15* (3), 170–180. https://doi.org/10.1038/s41565-020-0657-x.

(38) Walther, F.; Randau, S.; Schneider, Y.; Sann, J.; Rohnke, M.; Richter, F. H.; Zeier, W. G.; Janek, J. Influence of Carbon Additives on the Decomposition Pathways in Cathodes of Lithium Thiophosphate-Based All-Solid-State Batteries. *Chem. Mater.* **2020**, *32* (14), 6123–6136. https://doi.org/10.1021/acs.chemmater.0c01825.

(39) Zhang, W.; Leichtweiß, T.; Culver, S. P.; Koerver, R.; Das, D.; Weber, D. A.; Zeier, W. G.; Janek, J. The Detrimental Effects of Carbon Additives in $Li_{10}GeP_2S_{12}$ -Based Solid-State Batteries. *ACS Appl. Mater. Interfaces* **2017**, *9* (41), 35888–35896. https://doi.org/10.1021/acsami.7b11530.

Table of Contents

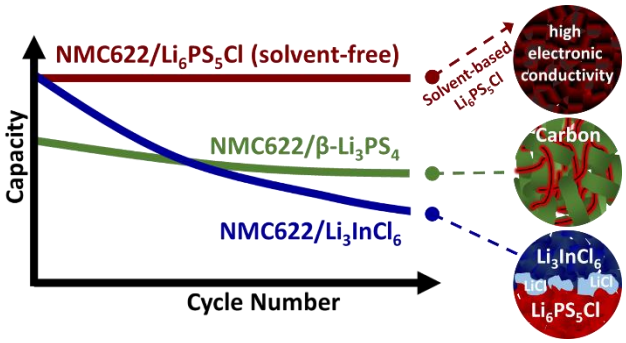

Graphic for manuscript